inorganics

MDPI

Article

Field-Induced Slow Magnetic Relaxation of Mono- and Dinuclear Dysprosium(III) Complexes Coordinated by a Chloranilate with Different Resonance Forms

Ryuta Ishikawa [1,*], Shoichi Michiwaki [1], Takeshi Noda [1], Keiichi Katoh [2], Masahiro Yamashita [2,3,4], Kouki Matsubara [1] and Satoshi Kawata [1]

1 Department of Chemistry, Faculty of Science, Fukuoka University, 8-19-1 Nanakuma, Jonan-ku, Fukuoka 814-0180, Japan; chem07inorg@gmail.com (S.M.); sd172011@cis.fukuoka-u.ac.jp (T.N.); kmatsuba@fukuoka-u.ac.jp (K.M.); kawata@fukuoka-u.ac.jp (S.K.)

2 Department of Chemistry, Graduate School of Science, Tohoku University, 6-3 Aramaki-Aza-Aoba, Aoba-ku, Sendai, Miyagi 980-8578, Japan; kkatoh@m.tohoku.ac.jp (K.K.); yamasita.m@gmail.com (M.Y.)

3 Advanced Institute for Materials Research (AIMR), Tohoku University, 2-1-1 Katahira, Aoba-ku, Sendai, Miyagi 980-8577, Japan

4 School of Materials Science and Engineering, Nankai University, Tianjin 300350, China

* Correspondence: ryutaishikawa@fukuoka-u.ac.jp; Tel.: +81-92-871-6631

Received: 14 November 2017; Accepted: 28 December 2017; Published: 30 December 2017

Abstract: We synthesized the dinuclear and mononuclear dysprosium(III) complexes $[\{Dy(Tp)_2\}_2(Cl_2An)]\cdot 2CH_2Cl_2$ (**1**) and $[Co(Cp)_2][Dy(Tp)_2(Cl_2An)]$ (**3**), where Cl_2An^{2-} and Tp^- are the chloranilate and hydrotris(pyrazolyl)borate ligand, respectively. In addition, the magnitude of the magnetic coupling between the lanthanide centers through the Cl_2An^{2-} bridge has been probed through the synthesis of $[\{Gd(Tp)_2\}_2(Cl_2An)]\cdot 2CH_2Cl_2$ (**2**), which is a gadolinium(III) analogue of **1**. Complexes **1**–**3** were characterized by infrared (IR) spectroscopy, elemental analysis, single-crystal X-ray diffraction, and SQUID measurements. IR and single-crystal X-ray structural analyses confirm that the coordination environments of the lanthanide(III) centers in **1** and **3** are similar to each other; i.e., eight-coordinated metal centers, each occupied by an N_6O_2 donor set from two Tp^- ligands and one Cl_2An^{2-} ligand. The coordination geometries of the lanthanide(III) centers in **1** and **2** are distorted triangular dodecahedral, while that in the mononuclear complex **3** is square antiprismatic, where the Cl_2An^{2-} ligand takes the bi-separated delocalized form in **1** and **2**, and the *o*-quinone form in **3**. Alternating-current (AC) magnetic studies clearly reveal that both **1** and **3** exhibit field-induced slow relaxations of magnetization that occur via Raman and direct processes. Complexes **1** and **3** exhibit different spin relaxation behavior, which reflects the coordination geometry around each Dy^{III} center and its nuclearity, as well as the molecular packing in the crystal lattice. Although the magnetic analysis of **2** revealed negligible magnetic coupling, Cl_2An^{2-} bridges with small biases may form in the dinuclear complexes, which play roles in the spin relaxation dynamics through dipolar interactions.

Keywords: single-ion magnets; single-molecule magnets; lanthanide ions; slow magnetic relaxation

1. Introduction

Molecule-based nanomagnets, such as single-molecule magnets (SMMs) [1–7] and single-ion magnets (SIMs) [8–12], are strictly low-dimensional magnetic systems that exhibit magnetization blocking at low temperatures, quantum tunneling of magnetization (QTM) [13], and quantum coherence [14,15]. Accordingly, SMMs have attracted a great deal of interest as promising candidates

for quantum computing [16], high-density information storage [17], and more recently, molecular spintronic materials [18–21].

Early surveys of SMMs were focused on polynuclear cluster complexes with high nuclearities due to the realization of large ground spin states [2]. However, it is rather difficult to combine a large ground spin state with a large magnetic anisotropy, since the entire molecular symmetry in a polynuclear cluster complex often increases with an increasing nuclearity, leading to a small magnetic anisotropy as a consequence. Therefore, the realization of polynuclear cluster complexes with large spin ground states and large magnetic anisotropies is still a significant challenge.

On the other hand, more recent frontline SMMs studies have tended to focus on enhancing magnetic anisotropy, rather than augmenting ground spin states, which is a much more informative method for increasing the blocking temperature and the activation energy barrier. From these perspectives, studies into SMMs, and more recently, SIMs, based on trivalent lanthanide (Ln^{III}), ions have proceeded at a rapid pace because of their significant magnetic anisotropies that arise from both spin-orbit coupling and crystal-field splitting, where crystal-field splitting is normally much smaller than spin–orbit coupling in Ln^{III} ions [22,23]. Hence, it is very important to investigate small changes in ligand-field strength associated with the coordination geometries of Ln^{III} ions. However, the relationship between the coordination geometry of the Ln^{III} ion and the slow magnetic relaxation of SMMs or SIMs is still largely unclear, because it is very difficult to systematically control the coordination geometries and the ligand-field strengths of Ln^{III} ions. We noticed that chloranilate (Cl_2An^{2-}) is a promising organic ligand for investigating the above-mentioned Ln^{III}-based SMMs or SIMs. The dianionic form of Cl_2An^{2-} has a delocalized π system with resonance structures that are represented by *p*-quinone, *o*-quinone, tetraquinone, and bi-separated delocalized forms (Scheme 1) [24,25]. The coordination geometry and the ligand-field strength of the central Ln^{III} ion can be fine-tuned by combining Cl_2An^{2-} with a suitable ancillary ligand, while maintaining a similar coordination environment. Hydrotris(pyrazolyl)borate (Tp^-) ligands are scorpionate ligands [26] that exhibit hard σ-donating characteristics and have been used to stabilize trivalent Ln^{III} metal centers. Thus, we chose Tp^- as the ancillary ligand.

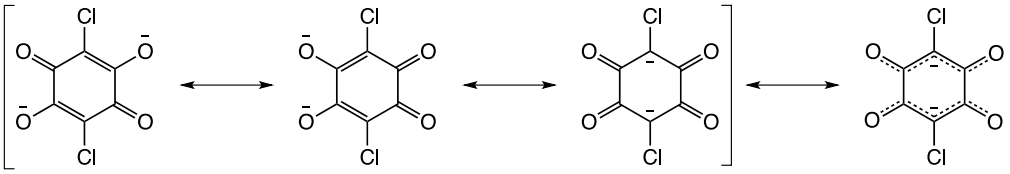

Scheme 1. Resonance structures in chloranilate (Cl_2An^{2-}).

Based on the above idea, we successfully synthesized mononuclear and dinuclear dysprosium(III) complexes bearing the Cl_2An^{2-} ligand and Tp^- as auxiliary ligands, in which the Cl_2An^{2-} ligand adopts the *o*-quinone and bi-separated delocalized forms, respectively. Comparisons of the spin-relaxation dynamics for the mononuclear and dinuclear complexes will aid in our understanding of dipolar interactions mediated by bridging Cl_2An^{2-} ligands in dinuclear complexes. Herein, we report the syntheses, single-crystal X-ray structures, and detailed magnetic properties of two types of complexes, namely $[\{Dy(Tp)_2\}_2(\mu\text{-}Cl_2An^{2-})]\cdot 2CH_2Cl_2$ and $[Co(Cp)_2][Dy(Tp)_2(Cl_2An^{2-})]$, which display slow magnetic relaxations under small static direct-current (DC) magnetic fields.

2. Results and Discussion

2.1. Syntheses and Characterizations

The $[\{Ln(Tp)_2\}_2(\mu\text{-}Cl_2An^{2-})]$ dinuclear complexes (**1**: Ln = Dy; **2**: Ln = Gd) are readily formed by the reaction of 4 equiv. of KTp and 1 equiv. of Na_2Cl_2An with 2 equiv. of the corresponding lanthanide chloride salt in water. The subsequent slow diffusion of hexane into a concentrated CH_2Cl_2

solution of **1** gave purple rod-shaped crystals, with two CH_2Cl_2 solvates per dinuclear unit, suitable for single-crystal X-ray diffraction studies [27]. On the other hand, reaction of **1** with 1 equiv. of cobaltocene ($Co(Cp)_2$, Cp^- = cyclopentadienide) in a N_2-filled glovebox led to the formation of the mononuclear $[Co(Cp)_2][Dy(Tp)_2(Cl_2An^{2-})]$ complex (**3**); **3** crystallized without any solvent molecules. Therefore, to the best of our knowledge, complexes **1**–**3** are the first heteroleptic systems containing the Cl_2An^{2-} and Tp^- ligands. Infrared (IR) spectroscopy provides complementary information to that obtained by single-crystal X-ray studies with respect to structural features (Figure 1). Complexes **1** and **2** have similar masses (162.5 amu for **1** and 157.25 amu for **2**), so large differences in their IR spectra were not observed, although some peaks are shifted. The IR absorptions associated with the bridging Cl_2An^{2-} ligand in both **1** and **2** are typified by predominant C–Cl and C–O vibrations at ~850 and 1528 cm^{-1}, respectively. In contrast, **3** has three characteristic absorption bands centered at 833, 1540, and 1643 cm^{-1}. The first two absorption bands are assigned to C–Cl and C–O vibrations, while the third absorption band is considered to correspond to C=O vibrations. This result is a promising indication that the Cl_2CA^{2-} ligand in **3** is in the *o*-quinone form [28]. Furthermore, the presence of the ancillary Tp^- ligands in **1**–**3** is confirmed by characteristic absorptions in their IR spectra at approximately 2470 cm^{-1} (c.f., KTp^-, νB–H = ~2440 cm^{-1}) [29].

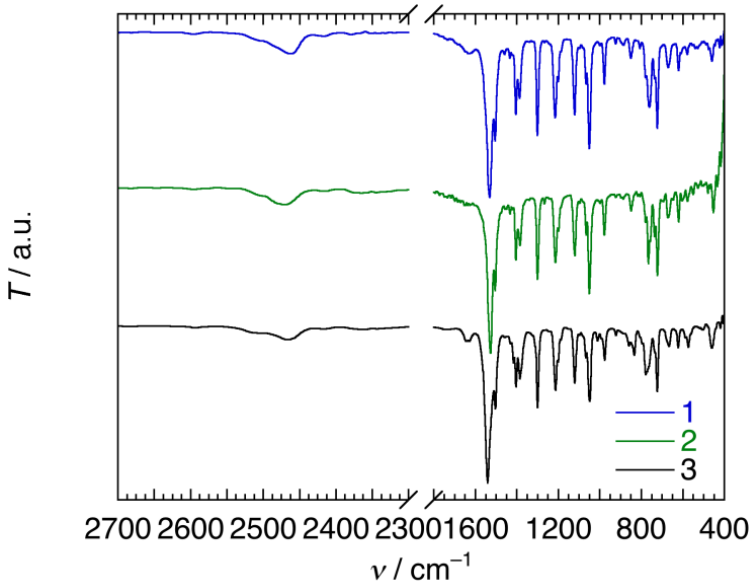

Figure 1. Infrared (IR) spectra for **1**–**3** at room temperature.

2.2. Molecular Structure Descriptions

The molecular structures of neutral dinuclear complexes **1** and **2** are isostructural and belong to the monoclinic $P2_1/n$ space group (No. 14) (Figure 2). Both **1** and **2** are centrosymmetric complexes with two Ln^{III} centers bridged by a bis-bidentate Cl_2An^{2-} ligand; consequently, only half of the dimer unit is unique. The coordination environments around the Ln^{III} centers in **1** and **2** are eight-coordinated with six N atoms from the two Tp^- capping ligands, and two O atoms from the Cl_2An^{2-} bridge. The eight-coordinate Ln^{III} centers adopt slightly distorted triangular dodecahedral geometries based on continuous shape measures (CShMs) [30,31] of 0.785 for **1** and 0.831 for **2**.

The bond distances within the rings of quinoidal ligands, such as Cl_2An^{2-}, bound to metal ions provide strong information about the electronic structures of the ligands (Scheme 1). The *o*-quinone form is usually found in mononuclear complexes through terminal bidentate coordination modes, whereas the bi-separated delocalized form is often found in polynuclear complexes and coordination polymers through bis-bidentate coordination modes. The C–O bond distances in the Cl_2An^{2-} ring of **1** are 1.255(2) Å and 1.259(2) Å , while the similar distances in **2** are 1.258(4) Å, and 1.261(4) Å.

The C–C bond distances are 1.393(3) Å, 1.396(3) Å, and 1.534(2) Å for **1**, and 1.389(5) Å, 1.393(5) Å, and 1.537(4) Å for **2**. These values confirm that the Cl_2An^{2-} bridging moieties in complexes **1** and **2** adopt the bi-separated delocalized forms, which also is strongly supported by the IR data. The respective intramolecular $Ln^{III}\cdots Ln^{III}$ distances through the Cl_2An^{2-} bridges are 8.6622(5) Å for **1** and 8.7042(5) Å for **2**. In addition, the shortest intermolecular Ln···Ln distances of 8.7398(5) Å for **1** and 8.9781(5) Å for **2** are comparable with the intramolecular distances.

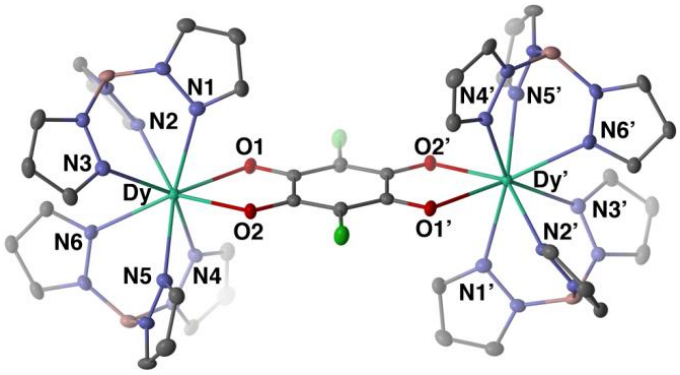

Figure 2. Molecular structure of **1**. H atoms and lattice solvent molecules are omitted for clarity.

The anionic mononuclear complex **3** cocrystallized with $[Co(Cp)_2]^+$ in its crystal lattice, and was found to belong to the monoclinic $P2_1/c$ space group (No. 14) (Figure 3). The coordination environment around the Dy^{III} center of the anionic monomer **3** is structurally similar to those in dimers **1** and **2**, differing only slightly in bond distances and angles. The eight-coordinate Dy^{III} center features a distorted square antiprismatic geometry, according to the CShM value of 1.116, in which the two square faces are defined by N1, N5, N9, and O1, and N3, N7, N11, and O2. The Cl_2An^{2-} moiety of **3** acts as a terminal capping ligand, unlike in dimers **1** and **2**. Hence, the resonance structure of Cl_2An^{2-} in the anionic monomer **3** differs significantly from those in **1** and **2** (vide supra). Indeed, the Cl_2An^{2-} C–O ring bond distances in **3** are 1.275(3) Å, 1.275(3) Å, 1.228(3) Å, and 1.234(3) Å, while the C–C bond distances are 1.376(4) Å, 1.382(4) Å, 1.419(4) Å, 1.427(4) Å, 1.519(3) Å, and 1.563(4) Å. These values clearly indicate both single and double-bond character. The Cl_2An^{2-} moiety in complex **3** is therefore in the *o*-quinone form. Finally, each anionic monomer in **3** is well separated in the crystal lattice, with closest intermolecular $Dy^{III}\cdots Dy^{III}$ distances of 9.5145(4) Å.

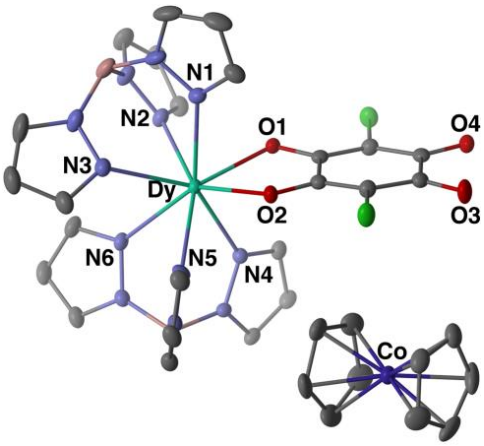

Figure 3. Molecular structure of **3**. H atoms are omitted for clarity.

2.3. Magnetic Properties

2.3.1. Static Magnetic Properties

DC magnetic susceptibility (χ_M) measurements on **1** were carried out in the 1.8–295 K temperature (T) range in an applied 0.1 T DC field (Figure 4). The value of $\chi_M T$ at 295 K for **1** was determined to be 28.29 $cm^3 \cdot K \cdot mol^{-1}$, which is in good agreement with the expected value of 28.34 $cm^3 \cdot K \cdot mol^{-1}$ for two uncoupled Dy^{III} ions ($^6H_{15/2}$ with $g = 4/3$). The $\chi_M T$ value remained constant over the 100–300 K T range, below which it decreased smoothly to a value of 23.83 $cm^3 \cdot K \cdot mol^{-1}$ at 1.8 K, due to the depopulation of excited Stark sublevels in the crystal-field state. The magnetization (M) of **1** increased rapidly with an increasing magnetic field (H) to 7 T (M = 10.55 μ_B) without saturation at 1.8 K, indicating very strong magnetic anisotropy (Figure S1, Supplementary Materials). Moreover, no hysteresis was observed for **1** above 1.8 K using a conventional SQUID. The detailed determination of the magnetic-exchange coupling constant (J), i.e., magnitude and sign (ferromagnetic or antiferromagnetic), of a polynuclear Ln complex is difficult because of its complicated 4f electronic structure. In contrast, the electronic structure of the Gd^{III} ion contains a half-filled 4f orbital system, leading to no orbital angular momentum, and can be analyzed as a simple spin-only case ($^8S_{7/2}$ with $g = 2$). Hence, the qualitative magnitude of J for **1** can be indirectly determined from that of the Gd^{III} analogue (**2**). T-dependent $\chi_M T$ measurements were performed in the 1.8–300 K T range in an applied DC magnetic field of 0.05 T (Figure 4). The $\chi_M T$ value of **2** was determined to be 15.75 $cm^3 \cdot K \cdot mol^{-1}$ at 300 K, which corresponds to the spin-only value of two uncoupled Gd^{III} ions with $g = 2.00$; the $\chi_M T$ value remained constant to 10 K. Further lowering of the temperature to 1.80 K lowered the $\chi_M T$ value to 15.02 $cm^3 \cdot K \cdot mol^{-1}$. Furthermore, the H-dependent isothermal M data at 1.8 K for **2** show a steady increase with increasing magnetic field, reaching saturation at a value of 14.0 μ_B at 7 T (Figure S1, Supplementary Materials). The magnetic behavior of **2** is the result of the competition between antiferromagnetic exchange between the Gd^{III} centers via the Cl_2An^{2-} bridge, and single-ion anisotropy arising from the Gd^{III} ion. To determine whether intermolecular isotropic magnetic exchange or single-ion magnetic anisotropy dominates, plots of $\chi_M T$ vs. T, and M vs. H for **2** were constructed using the spin Hamiltonian given by Equation (1):

$$\begin{aligned} \hat{\mathcal{H}} &= \hat{\mathcal{H}}_{HDVV} + \hat{\mathcal{H}}_{ZFS} + \hat{\mathcal{H}}_{Zeeman} \\ &= -2J_{Gd1-Gd2}\hat{S}_{Gd1} \cdot \hat{S}_{Gd2} + 2D_{Gd}\left[\hat{S}^2_{Gd,\,z} - \frac{S_{Gd}(S_{Gd}+1)}{3}\right] + 2E_{Gd}\left(\hat{S}^2_{Gd,\,x} - \hat{S}^2_{Gd,\,y}\right) + g\mu_B\hat{S}_T\vec{H} \end{aligned} \quad (1)$$

where S_{Gd1} and S_{Gd2} are the spin operators for Gd^{III} ions ($S = 7/2$), $J_{Gd1–Gd2}$ is the isotropic magnetic exchange coupling constant between two Gd^{III} centers, D_{Gd} and E_{Gd} are the axial and rhombic zero-field splitting (ZFS) parameters that are associated with an $S = 7/2$ Gd^{III} ion, respectively, g is the isotropic g factor, and μ_B is the Bohr magneton. This model fitted the $\chi_M T$ vs. T plot well over the entire 1.8 to 300 K temperature range, and the M vs. H plot at 1.80 K yielded $J_{Gd1–Gd2}/k_B = -0.0066$ K, $D_{Gd}/k_B = 0.17$ K, and $E_{Gd}/k_B = 1.1 \times 10^{-5}$ (≈ 0) K, with $g = 2.00$ (Figures 4 and S1, Supplementary Materials). The calculated g factor is close to the spin-only value, and a negligible antiferromagnetic interaction between the two Gd^{III} centers through the Cl_2An^{2-} bridge, and a large ZFS contribution ($|D| >> |J|$) were found for **2**. Except for organic radical bridging ligands, magnetic interactions between paramagnetic Ln^{III} centers via common organic bridging ligands are well-known to be very weak in general, because 4f orbitals are shielded by outer 6s and 5d orbitals. The two Gd^{III} centers in **2** are also well-separated by a diamagnetic spacer, namely the Cl_2An^{2-} bridge (vide supra). Therefore, the small calculated J value might be meaningless. As an alternative, we subsequently attempted to fit the magnetic data for **2** by considering only single-ion anisotropy with the mean-field approximation (zJ'), as given by Equation 2:

$$\begin{aligned} \hat{\mathcal{H}} &= \hat{\mathcal{H}}_{ZFS} + \hat{\mathcal{H}}_{Zeeman} + \hat{\mathcal{H}}_{MFA} \\ &= 2D_{Gd}\left[\hat{S}^2_{Gd,\,z} - \frac{S_{Gd}(S_{Gd}+1)}{3}\right] + 2E_{Gd}\left(\hat{S}^2_{Gd,\,x} - \hat{S}^2_{Gd,\,y}\right) + g\mu_B\hat{S}_T\vec{H} - zJ'\langle\hat{S}_T\rangle\hat{S}_T \end{aligned} \quad (2)$$

This model also fitted the $\chi_M T$ vs. T plot well over the entire 1.8 to 300 K temperature range, and the M vs. H plot at 1.80 K provided D_{Gd}/k_B = 0.18 K, E_{Gd}/k_B = 1.8 × 10^{-4} (≈ 0) K, and g = 2.00 with a negligible zJ'/k_B value (~−10^{-5} K). Hence, the $\chi_M T$ value for **3** at 300 K is 14.16 $cm^3 \cdot K \cdot mol^{-1}$, which is in good agreement with that of the free Dy^{III} ion ($^6H_{15/2}$ with g = 4/3). The $\chi_M T$ product gradually decreased with decreasing T, and finally reached a minimum value of 11.87 $cm^3 \cdot K \cdot mol^{-1}$ at 1.8 K. This magnetic behavior is ascribable to the thermal depopulation of the crystal-field state. The M vs. H plot of **3** at 1.8 K displays significant magnetic anisotropy and does not reach saturation up to 7 T (M = 5.10 μ_B).

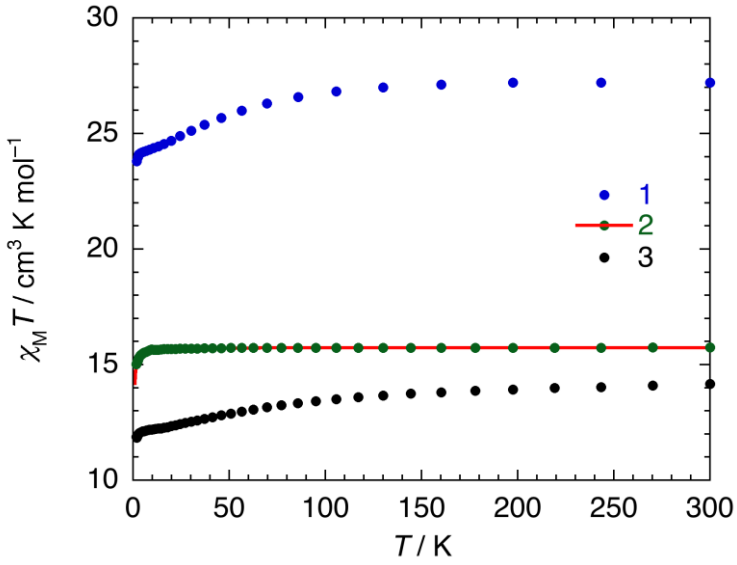

Figure 4. T dependence of $\chi_M T$ products for **1**–**3**. The solid red line represents fit to the data, which is described in the text.

2.3.2. Dynamic Magnetic Properties

To study the slow relaxation of the magnetization of both **1** and **3**, alternate-current (AC) susceptibility measurements were performed at a fixed T of 1.8 K with a DC field (H_{DC}) that varied between 0 and 8000 Oe (Figures 5 and 6). The χ_M″ signals for **1** and **3** in the absence of an applied field increased with increasing frequency (ν), but exhibited only tailing, and no apparent peaks were observed due to blocking in the available ν range. Subsequently, ν-dependent non-zero χ_M″ signals clearly appeared at small static H_{DC}. This result clearly indicates that zero-field QTM [13] and/or dipolar interactions [32] are suppressed, and/or the non-negligible transverse magnetic anisotropy [33] is broken by the application of H_{DC} in the ground state. Each χ_M″ peak maximum for **1** shifted to lower ν with an increasing applied H_{DC} up to ~950 Oe. Further increases in H_{DC} resulted in the maximum χ_M″ shifting to higher ν. Similarly, the maximum χ_M″ value for **3** shifted to lower ν, reaching a minimum at ~1500 Oe, above which it shifted to higher ν. Therefore, the optimum H_{DC} values for **1** and **3** were determined to be ~950 Oe for **1** and ~1500 Oe for **3**, which was used in the T- and ν-dependent AC susceptibility experiments (Figures 7, 8 and S2, Supplementary Materials).

In addition, the other striking feature for both **1** and **3** is the clear presence of two distinct relaxation processes at higher H_{DC} fields: the H_{DC}-dependent component and the H_{DC}-independent component, which are thermal and QTM relaxation modes, respectively (Figure 6).

Both **1** and **3** show ν-dependent χ_M″ at their respective optimum H_{DC}. The relaxation time (τ) can be extracted at each blocking temperature using a generalized Debye model (Figure 7). Here, Argand plots [34] (χ_M′ vs. χ_M″ plot) for **1** and **3** were semicircular with small α parameters in the 0.0063–0.31 range for **1** and the 0.035–0.44 range for **3** (Figure 8).

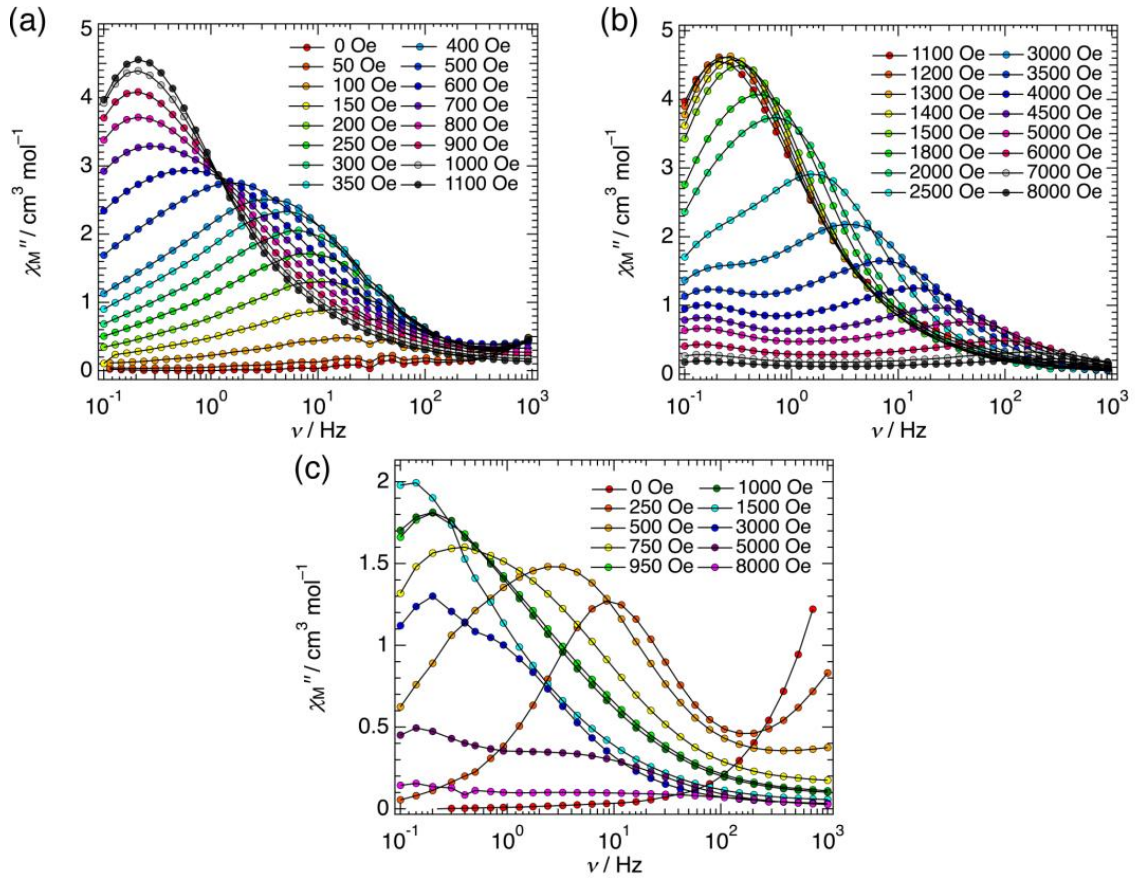

Figure 5. Variable-field χ_M'' for **1** (**a** and **b**) and **3** (**c**) at 1.8 K for direct-current (DC) fields of 0–8000 Oe, over the frequency range of 0.1–1000 Hz. Solid black lines serve as guides.

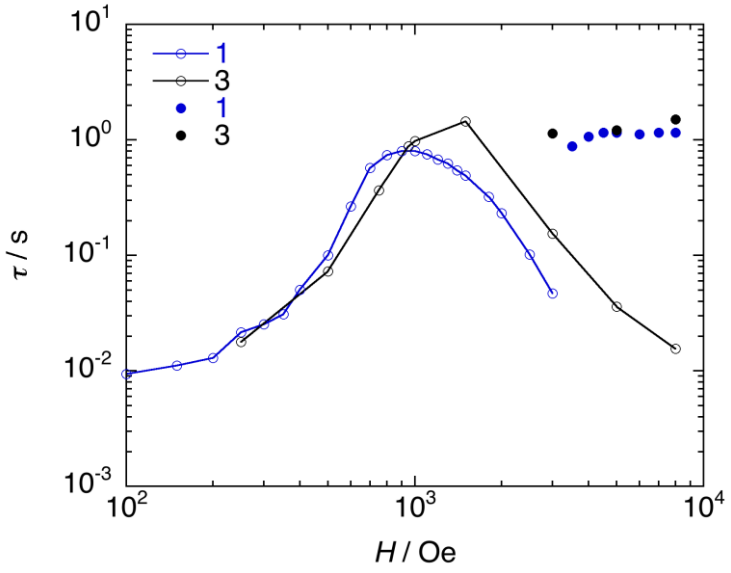

Figure 6. H_{DC}-dependece of τ for **1** and **3** at 1.8 K indicating two distinct relaxation processes: H_{DC}-dependent component (blue open circles for **1** and blue open circles for **3**) and H_{DC}-independent ones (blue filled circles for **1** and black filled circles for **3**). Solid lines serve as guides.

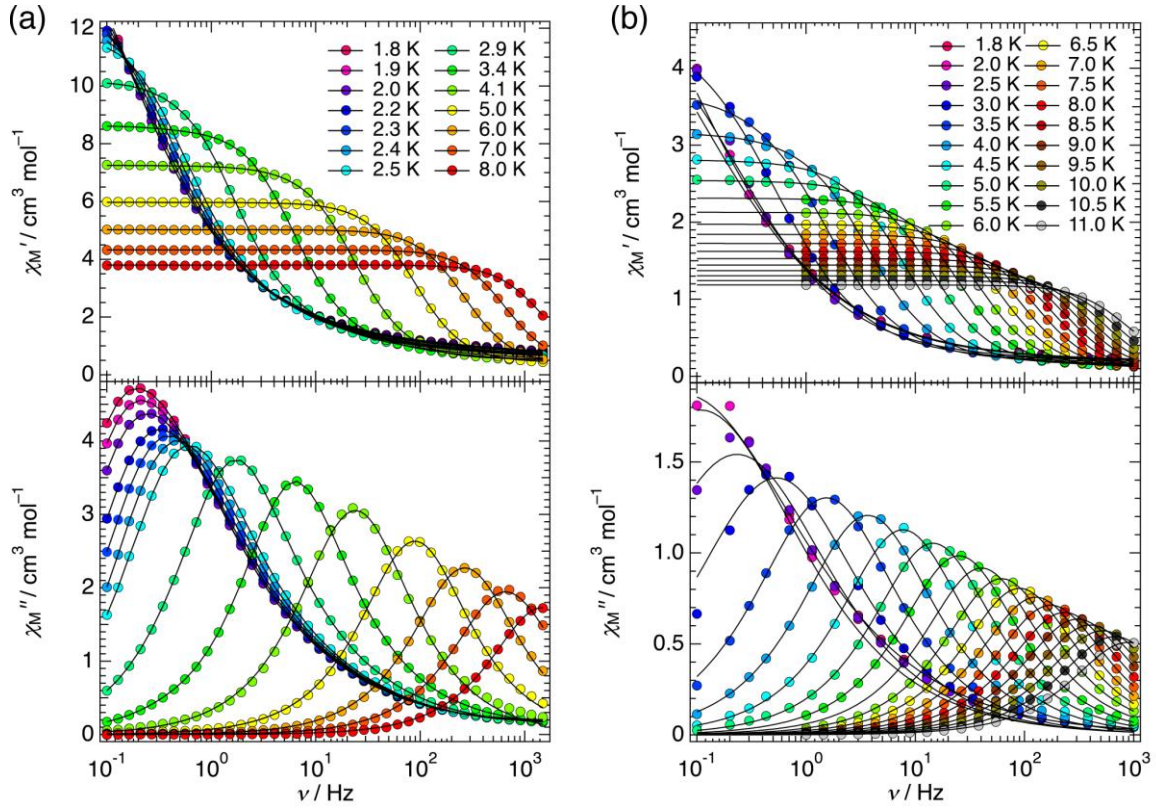

Figure 7. ν-dependent χ_M' and χ_M'' in the T range 1.8–8.0 K in an applied H_{DC} of 950 Oe for **1** (**a**) and in the T range 1.8–11.0 K in an applied H_{DC} of 1500 Oe for **3** (**b**), respectively. Solid black lines represent best fits to a generalized Debye model.

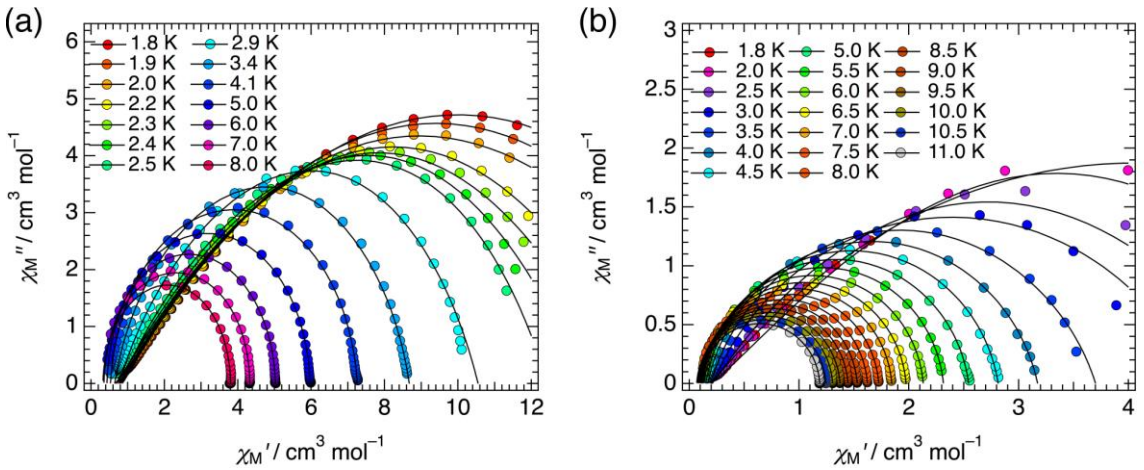

Figure 8. Argand plots at given temperatures in an applied DC field of 950 Oe for **1** (**a**) and 1500 Oe for **3** (**b**), respectively. Solid black lines are best-fit lines.

The linear regions at higher T in the semi-logarithmic plots of τ vs. $1/T$ (Arrhenius plots) for **1** and **3** were used to calculate the thermal energy barrier (Δ_{eff}) for magnetization reversal, known as Orbach relaxation [35], which provided Δ_{eff}/k_B = 44.7 K and $\tau_0 = 3.43 \times 10^{-7}$ s for **1**, and Δ_{eff}/k_B = 49.4 K and $\tau_0 = 2.12 \times 10^{-6}$ s for **2** (Figure 9). However, the Arrhenius plots for **1** and **3** deviate from linearity at lower T. Such magnetic relaxation behavior for **1** and **3** suggests the coexistence of

thermal relaxation processes and other operative relaxation processes. Hence, τ for **1** and **3** in the given temperature range were analyzed by Equation 3:

$$\tau^{-1} = \tau_0^{-1} \exp\left(-\frac{\Delta_{\text{eff}}}{k_B T}\right) + CT^n + AT + \tau_{\text{QTM}} \quad (3)$$

where the first, second, third, and fourth terms represent Orbach, Raman [35–39], direct [35–39], and QTM processes, respectively. Data for **1** and **3** were analytically reproduced using Equation 3 with appropriate terms for the Raman and direct processes. The best fit was obtained with $C = 6.12 \times 10^{-3}$ $s^{-1}{\cdot}K^{-7.02}$ and $A = 0.323$ $s^{-1}{\cdot}K^{-1}$ for **1**, while $C = 7.22 \times 10^{-3}$ $s^{-1}{\cdot}K^{-5.71}$ and $A = 0.106$ $s^{-1}{\cdot}K^{-1}$ were best for **3** (Figure 9). Generally, the power index (n) of T for a Raman process is 9 because of Kramers ions. The n values of **1** and **3** are lower than the expected value, which might be attributable to the involvement of both optical and acoustic Raman processes during magnetic relaxation [38]. Therefore, both Raman and direct processes dominate the spin dynamics of **1** and **3**. Complexes **1** and **3** exhibit different spin-relaxation behavior, which reflect the coordination geometries around their Dy^{III} centers and their nuclearities, as well as crystal-lattice molecular packing. In addition, although the magnetic analysis of **2** did not reveal any magnetic exchange coupling via the Cl_2An^{2-} ligand, the dinuclear complex **1** might create a small bias that allows for tunneling at zero field.

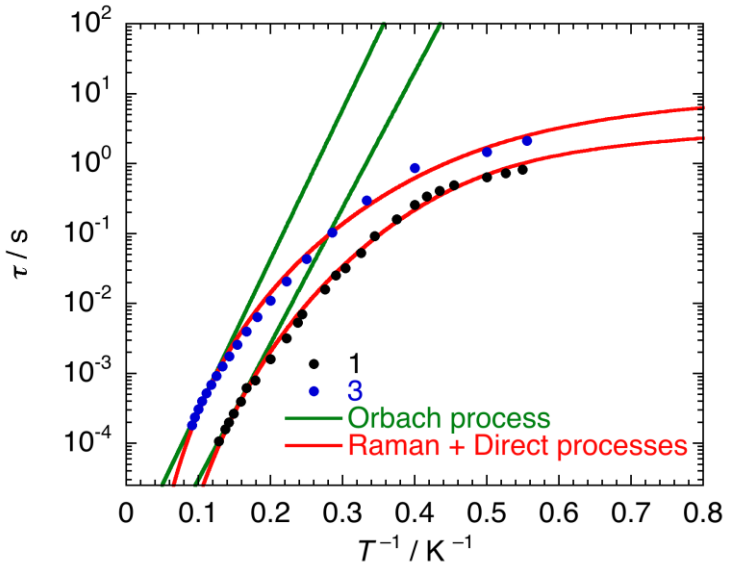

Figure 9. T-dependece of τ for **1** and **3** at 950 and 1500 Oe, respectively. Solid lines were fitted to the data as described in the text.

3. Experimental Section

3.1. Materials and Methods

$Co(Cp)_2$, $DyCl_3{\cdot}6H_2O$, $GdCl_3{\cdot}6H_2O$, $Na_2Cl_2An{\cdot}3H_2O$, and all of the solvents were purchased from Wako Pure Chemical Industries, Ltd. (Osaka, Japan) KTp was purchased from Tokyo Chemical Industry (TCI) Co., Ltd. (Tokyo, Japan). All of the chemicals were reagent grade and were used as received. Both CH_2Cl_2 and hexane were super dehydrated grade and deoxidized grade. Unless otherwise noted, reactions and subsequent manipulations were performed under aerobic conditions at room temperature, while compound **3** was prepared under an inert N_2 atmosphere using standard glovebox techniques.

3.2. Synthesis of [{Dy(Tp)$_2$}$_2$(μ-Cl$_2$An)]·2CH$_2$Cl$_2$ (**1**)

This complex was prepared from modification of the original method of Kaizaki et al. [26]. An aqueous solution (5 mL) of $DyCl_3 \cdot 6H_2O$ (75.4 mg, 0.2 mmol) was added dropwise to a stirred aqueous solution (5 mL) of $Na_2Cl_2An \cdot 3H_2O$ (30.7 mg, 0.1 mmol) and KTp (100.8 mg, 0.4 mmol), resulting in a fine purple precipitate immediately. After stirring for 10 min, the purple solid was isolated via filtration, washed with a small amount of H_2O (2 × 5 mL) and Et_2O (3 × 5 mL), and dried in vacuo. The purple solid was then dissolved in CH_2Cl_2, and the resultant purple solution was filtered. Diffusion of hexane into the filtrate yielded purple rod-shaped crystals suitable for single-crystal X-ray diffraction analysis within 1 week. Yield: 144.5 mg (52%). Anal. Calcd. for $C_{44}H_{44}B_4Cl_6Dy_2N_{24}O_4$: C, 34.01; H, 2.85; N, 21.63%. Found: C, 33.98; H, 2.90; N, 21.72%.

3.3. Synthesis of [{Gd(Tp)$_2$}$_2$(μ-Cl$_2$An)]·2CH$_2$Cl (**2**)

This complex was prepared according to the same method as that for 1 with $GdCl_3 \cdot 6H_2O$ instead of $DyCl_3 \cdot 6H_2O$. Yield: 48%. $C_{44}H_{44}B_4Cl_6Gd_2N_{24}O_4$: calcd. C 34.24, H 2.87, N 21.78; found C 34.56, H 2.91, N 21.94.

3.4. Synthesis of [Co(Cp)$_2$][Dy(Tp)$_2$(Cl$_2$An)] (**3**)

In a N_2-filled glovebox, $Co(Cp)_2$ dissolved in PhMe (5 mL) was added to a solution of **1** in the same solvent (5 mL). The color of the reaction mixture changed to yellowish green. Upon stirring the mixture, bright yellow microcrystalline solid appeared immediately, which was collected by filtration, washed with a small amount of Et_2O (5 mL), and allowed to dry on the filter for 15 min. The yellowish green solid was then dissolved in MeCN, and the resulting pale yellow solution was filtered. Slow diffusion of Et_2O into the filtrate gave red block-shaped crystals suitable for single-crystal X-ray diffraction analysis for two weeks. Yield: 83%. Anal. Calc. for $C_{34}H_{30}B_2Cl_2CoDyN_{12}O_4$: C, 41.47; H, 3.07; N, 17.07. Found: C, 41.33; H, 3.14; N, 16.87%.

3.5. Single-crystal X-ray Crystallography Data Collection and Refinement

Single-crystals of **1**, **2**, and **3** were coated with Nujol and were quickly mounted on MicroLoops (MiTeGen LLC., Ithaca, NY, USA) and immediately cooled in a N_2 cold stream to avoid decomposition. Data collection was performed on a Rigaku R-AXIS RAPID II IP diffractometer (Rigaku Corporation, Tokyo, Japan) with graphite-monochromated Mo Kα radiation (λ = 0.71075 Å) and a low-temperature apparatus. The crystal dimensions for **1**, **2**, and **3** were 0.60 × 0.15 × 0.10, and 0.50 × 0.10 × 0.10, and 0.60 × 0.20 × 0.10 mm, respectively. Data for **1**, **2**, and **3** were collected at 163(1), 100(1) and 108(1)K, respectively. Data integration, preliminary data analysis, and absorption corrections were performed using the Rigaku CrystalClear-SM 1.4.0 SP1 [40] and the CrystalStructure 4.1.1 [41] crystallographic software packages. The molecular structures were solved using direct methods included in SIR2011 [42] and refined using the *SHELXL* program [43]. All nonhydrogen atoms were refined anisotropically. All hydrogen atoms were introduced as fixed contributors. CCDC-1584512, -1584513 and -1584514 for **1**, **2**, and **3** contain the supplementary crystallographic data for this paper, and can be obtained free of charge from The Cambridge Crystallographic Data Centre via www.ccdc.cam.ac.uk/data_request/cif.

3.6. Physical Measurements

Elemental analyses were performed by the Technical Support Division, Research and Analytical Centre for Giant Molecules, Graduate School of Science, Tohoku University. Fourier transform infrared (FTIR) spectra were acquired as KBr disks at room temperature on a JASCO FT/IR-410 spectrophotometer (JASCO Corporation, Tokyo, Japan). Magnetic data were collected on a Quantum Design MPMS3 or MPMS-5S superconducting quantum interference device (SQUID) magnetometer (Quantum Design Japan, Inc., Tokyo, Japan). All of the magnetic measurements were performed on finely ground microcrystalline powders in a calibrated gelatin capsule. DC

susceptibility measurements were performed in the *T* range of 1.8–300 K in a DC field of 0.05 T or 0.1 T. Field-dependent dc magnetization measurements were performed from −7 to +7 T at 1.8 K. AC susceptibility measurements were performed in the *T* range of 1.8–20 K in a 3 Oe AC field, oscillating at frequencies of 1 and 997 or 1488 Hz in different applied DC fields. Magnetic susceptibility data were corrected for diamagnetic contributions from the sample holder as well as for the core diamagnetism of each sample estimated using Pascal's constants [44].

4. Conclusions and Outlook

The dinuclear and mononuclear [{Dy(Tp)$_2$}$_2$(μ-Cl$_2$An)] and [Co(Cp)$_2$][Dy(Tp)$_2$(Cl$_2$An)] eight-coordinate complexes were synthesized. The two complexes have similar N_6O_2 coordination environments that are based on the dianionic Cl_2An^{2-} ligand and Tp^- as auxiliary ligands. However, each Cl_2An^{2-} moiety adopts the bi-separated delocalized form in dinuclear [{Dy(Tp)$_2$}$_2$(μ-Cl$_2$An)], and the *o*-quinone form in mononuclear [Co(Cp)$_2$][Dy(Tp)$_2$(Cl$_2$An)]. Therefore, in this work, both complexes were magnetically characterized to examine how the donor strength affects the slow relaxation of the magnetization. Dynamic magnetic measurements clearly reveal that both of the complexes exhibit temperature-dependent slow relaxations of magnetization facilitated by multiple relaxation pathways. Their spin dynamics are different, reflecting the coordination geometries around the Dy^{III} centers and their nuclearities, as well as crystal-lattice molecular packing. The redox-active Cl_2An^{2-} ligand is a good candidate for the future construction of redox-switchable SMMs, as anilate derivatives readily undergo redox reactions to form both diamagnetic and paramagnetic species; such redox-switchable SMMs and/or SIMs that may be applied in future technologies, such as molecular spintronics. Furthermore, we are currently constructing dinuclear complexes of all other lanthanides bridged with the Cl_2An^{2-} moiety. This effort will provide valuable insight into the electronic structures, magnetic properties, and trends observed in the series of dinuclear [{Ln(Tp)$_2$}$_2$(μ-Cl$_2$An)] complexes.

Supplementary Materials: The following are available online at www.mdpi.com/2304-6740/6/1/7/s1. Cif and cif-checked files. Figure S1: Field dependence of magnetization plots of **1**–**3** at 1.8 K. The solid red lines were fitted to the data as described in the text.; Figure S2: Temperature dependence of χ_M' and χ_M'' products at given frequencies in an applied DC field of 950 Oe for **1** and 1500 Oe for **3**, respectively. Solid black lines serve as guides.

Acknowledgments: This work was partially supported by JSPS KAKENHI (Grant-in-Aid for Scientific Research (C) and Coordination Asymmetry) Grant Numbers 16K05735 and 17H05390 (Ryuta Ishikawa and Satoshi Kawata), the Central Research Institute of Fukuoka University Grant Numbers 171041 (Ryuta Ishikawa) and 171011 (Satoshi Kawata).

Author Contributions: Ryuta Ishikawa conceived and designed the experiment; Ryuta Ishikawa, Shoichi Michiwaki, Takeshi Noda, Kouki Matsubara and Satoshi Kawata executed the synthesis and characterization; Ryuta Ishikawa, Keiichi Katoh and Masahiro Yamashita executed magnetic measurements; Ryuta Ishikawa analyzed the all data and wrote the paper.

Conflicts of Interest: The authors declare no conflict of interest.

References

1. Sessoli, R.; Gatteschi, D.; Caneschi, A.; Novak, M.A. Magnetic bistability in a metal-ion cluster. *Nature* **1993**, *365*, 141–143. [CrossRef]
2. Christou, G.; Gatteschi, D.; Hendrickson, D.N.; Sessoli, R. Single-molecule magnets. *MRS Bull.* **2000**, *25*, 66–71. [CrossRef]
3. Gatteschi, D.; Sessoli, R.; Villain, J. *Molecular Nanomagnets*; Oxford University Press: Oxford, UK, 2006.
4. Jeon, I.-R.; Clerac, R. Controlled association of single-molecule magnets (SMMs) into coordination networks: towards a new generation of magnetic materials. *Dalton. Trans.* **2012**, *41*, 9569–9586. [CrossRef] [PubMed]
5. Demir, S.; Jeon, I.-R.; Long, J.R.; Harris, T.D. Radical ligand-containing single-molecule magnets. *Coord. Chem. Rev.* **2015**, *289–290*, 149–176. [CrossRef]
6. Sessoli, R.; Powell, A.K. Strategies towards single molecule magnets based on lanthanide ions. *Coord. Chem. Rev.* **2009**, *253*, 2328–2341. [CrossRef]

7. Woodruff, D.N.; Winpenny, R.E.P.; Layfield, R.A. Lanthanide single-molecule magnets. *Chem. Rev.* **2013**, *113*, 5110–5148. [CrossRef] [PubMed]
8. Craig, G.A.; Murrie, M. 3d Single-ion magnets. *Chem. Soc. Rev.* **2015**, *44*, 2135–2147. [CrossRef] [PubMed]
9. Frost, J.M.; Harriman, K.L.M.; Murugesu, M. The rise of 3-d single-ion magnets in molecular magnetism: towards materials from molecules? *Chem. Sci.* **2016**, *7*, 2470–2491. [CrossRef] [PubMed]
10. Bar, A.K.; Pichon, C.; Sutter, J.-P. Magnetic anisotropy in two- to eight-coordinated transition–metal complexes: Recent developments in molecular magnetism. *Coord. Chem. Rev.* **2016**, *308*, 346–380. [CrossRef]
11. Meng, Y.S.; Jiang, S.D.; Wang, B.W.; Gao, S. Understanding the magnetic anisotropy toward single-ion magnets. *Acc. Chem. Res.* **2016**, *49*, 2381–2389. [CrossRef] [PubMed]
12. McAdams, S.G.; Ariciu, A.-M.; Kostopoulos, A.K.; Walsh, J.P.S.; Tuna, F. Molecular single-ion magnets based on lanthanides and actinides: Design considerations and new advances in the context of quantum technologies. *Coord. Chem. Rev.* **2017**, *346*, 216–239. [CrossRef]
13. Gatteschi, D.; Sessoli, R. Quantum Tunneling of Magnetization and Related Phenomena in Molecular Materials. *Angew. Chemie Int. Ed.* **2003**, *42*, 268–297. [CrossRef] [PubMed]
14. Schlegel, C.; van Slageren, J.; Manoli, M.; Brechin, E.K.; Dressel, M. Direct observation of quantum coherence in single-molecule magnets. *Phys. Rev. Lett.* **2008**, *101*, 147203. [CrossRef] [PubMed]
15. Bader, K.; Dengler, D.; Lenz, S.; Endeward, B.; Jiang, S.-D.; Neugebauer, P.; van Slageren, J. Room temperature quantum coherence in a potential molecular qubit. *Nat. Commun.* **2014**, *5*, 5304. [CrossRef] [PubMed]
16. Leuenberger, M.N.; Loss, D. Quantum computing in molecular magnets. *Nature* **2001**, *410*, 789–793. [CrossRef] [PubMed]
17. Mannini, M.; Pineider, F.; Sainctavit, P.; Danieli, C.; Otero, E.; Sciancalepore, C.; Talarico, A.M.; Arrio, M.-A.; Cornia, A.; Gatteschi, D.; Sessoli, R. Magnetic memory of a single-molecule quantum magnet wired to a gold surface. *Nat. Mater.* **2009**, *8*, 194–197. [CrossRef] [PubMed]
18. Bogani, L.; Wernsdorfer, W. Molecular spintronics using single-molecule magnets. *Nat. Mater.* **2008**, *7*, 179. [CrossRef] [PubMed]
19. Camarero, J.; Coronado, E. Molecular vs. inorganic spintronics: the role of molecular materials and single molecules. *J. Mater. Chem.* **2009**, *19*, 1678–1684. [CrossRef]
20. Sanvito, S. Molecular spintronics. *Chem. Soc. Rev.* **2011**, *40*, 3336–3355. [CrossRef] [PubMed]
21. Clemente-Juan, J.M.; Coronado, E.; Gaita-Arino, A. Magnetic polyoxometalates: from molecular magnetism to molecular spintronics and quantum computing. *Chem. Soc. Rev.* **2012**, *41*, 7464–7478. [CrossRef] [PubMed]
22. Sorace, L.; Benelli, C.; Gatteschi, D. Lanthanides in molecular magnetism: old tools in a new field. *Chem. Soc. Rev.* **2011**, *40*, 3092–3104. [CrossRef] [PubMed]
23. Liddle, S.T.; van Slageren, J. Improving f-element single molecule magnets. *Chem. Soc. Rev.* **2015**, *44*, 6655–6669. [CrossRef] [PubMed]
24. Kitagawa, S.; Kawata, S. Coordination compounds of 1,4-dihydroxybenzoquinone and its homologues. Structures and properties. *Coord. Chem. Rev.* **2002**, *224*, 11–34. [CrossRef]
25. Mercuri, M.L.; Congiu, F.; Concas, G.; Sahadevan, S.A. Recent advances on anilato-based molecular materials with magnetic and/or conducting properties. *Magnetochemistry* **2017**, *3*, 1. [CrossRef]
26. Trofimenko, S. Recent advances in poly(pyrazolyl)borate (scorpionate) chemistry. *Chem. Rev.* **1993**, *93*, 943–980. [CrossRef]
27. Abdus Subhan, M.; Kawahata, R.; Nakata, H.; Fuyuhiro, A.; Tsukuda, T.; Kaizaki, S. Synthesis, structure and spectroscopic properties of chloranilate-bridged 4f–4f dinuclear complexes: A comparative study of the emission properties with Cr–Ln complexes. *Inorganica Chim. Acta* **2004**, *357*, 3139–3146. [CrossRef]
28. Ishikawa, R.; Horii, Y.; Nakanishi, R.; Ueno, S.; Breedlove, B.K.; Yamashita, M.; Kawata, S. Field-induced single-ion magnetism based on spin-phonon relaxation in a distorted octahedral high-spin cobalt(II) complex. *Eur. J. Inorg. Chem.* **2016**, *2016*, 3233–3239. [CrossRef]
29. Apostolidis, C.; Rebizant, J.; Kanellakopulos, B.; von Ammon, R.; Dornberger, E.; Müller, J.; Powietzka, B.; Nuber, B. Homoscorpionates (hydridotris(1-pyrazolyl)borato complexes) of the trivalent 4f ions. The crystal and molecular structure of $[(HB(N_2C_3H_3)_3)_3Ln^{III}$, (Ln = Pr, Nd). *Polyhedron* **1997**, *16*, 1057–1068. [CrossRef]
30. Casanova, D.; Alemany, P.; Bofill, J.M.; Alvarez, S. Shape and symmetry of heptacoordinate transition-metal complexes: Structural trends. *Chem. Eur. J.* **2003**, *9*, 1281–1295. [CrossRef] [PubMed]
31. Alvarez, S.; Alemany, P.; Casanova, D.; Cirera, J.; Llunell, M.; Avnir, D. Shape maps and polyhedral interconversion paths in transition metal chemistry. *Coord. Chem. Rev.* **2005**, *249*, 1693–1708. [CrossRef]

32. Guo, Y.-N.; Xu, G.-F.; Wernsdorfer, W.; Ungur, L.; Guo, Y.; Tang, J.; Zhang, H.-J.; Chibotaru, L.F.; Powell, A.K. Strong axiality and ising exchange interaction suppress zero-field tunneling of magnetization of an asymmetric Dy_2 single-molecule magnet. *J. Am. Chem. Soc.* **2011**, *133*, 11948–11951. [CrossRef] [PubMed]
33. Ungur, L.; Chibotaru, L.F. Magnetic anisotropy in the excited states of low symmetry lanthanide complexes. *Phys. Chem. Chem. Phys.* **2011**, *13*, 20086–20090. [CrossRef] [PubMed]
34. Cole, K.S.; Cole, R.H. Dispersion and absorption in dielectrics I. Alternating current characteristics. *J. Chem. Phys.* **1941**, *9*, 341–351. [CrossRef]
35. Orbach, R. Spin-lattice relaxation in rare-earth salts. *Proc. R. Soc. Lond. A Math. Phys. Eng. Sci.* **1961**, *264*, 458–484. [CrossRef]
36. Orbach, R. On the theory of spin-lattice relaxation in paramagnetic salts. *Proc. Phys. Soc.* **1961**, *77*, 821–826. [CrossRef]
37. Abragam, A.; Bleaney, B. *Electron Paramagnetic Resonance of Transition Ions*; Clarendon Press: Oxford, UK, 1970.
38. Shrivastava, K.N. Theory of spin–lattice relaxation. *Phys. Status Solidi* **1983**, *117*, 437–458. [CrossRef]
39. Scott, P.L.; Jeffries, C.D. Spin-lattice relaxation in some rare-earth salts at helium temperatures; observation of the phonon bottleneck. *Phys. Rev.* **1962**, *127*, 32–51. [CrossRef]
40. *CrystalClear-SM*; Version 1.4.0 SP1; Rigaku and Rigaku/MSC: The Woodlands, TX, USA, 2008.
41. *CrystalStructure*; Version 4.1.1; Rigaku and Rigaku/MSC: The Woodlands, TX, USA, 2015.
42. Burla, M.C.; Caliandro, R.; Camalli, M.; Carrozzini, B.; Cascarano, G.L.; Giacovazzo, C.; Mallamo, M.; Mazzone, A.; Polidori, G.; Spagna, R. *SIR2011*: A new package for crystal structure determination and refinement. *J. Appl. Crystallogr.* **2012**, *45*, 357–361. [CrossRef]
43. Sheldrick, G.M. A short history of *SHELX*. *Acta Crystallogr. Sect. A* **2008**, *64*, 112–122. [CrossRef] [PubMed]
44. Kahn, O. *Molecular Magnetism*; VCH: Weinheim, Germany, 1993.